frontiers in Earth Science

ORIGINAL RESEARCH
published: 17 March 2022
doi: 10.3389/feart.2022.833918

Mechanism of Faster CH_4 Bubble Growth Under Surface Waves in Muddy Aquatic Sediments: Effects of Wave Amplitude, Period, and Water Depth

*Abhishek Painuly and Regina Katsman**

Dr. Moses Strauss Department of Marine Geosciences, Leon H. Charney School of Marine Science, University of Haifa, Haifa, Israel

Methane (CH_4) transport from organic-rich fine-grained (muddy) shallow aquatic sediments to water column is mediated dominantly by discrete bubbles, which is an important natural source of greenhouse CH_4. The lifespan of these bubbles within the sediment comprises two successive stages: growth from nucleation up to a mature size and then buoyant ascent toward the sediment–water interface. Bubbles often experience an oscillating overburden load due to the passage of winds and/or storm-induced short period surface waves or long-period tides, which can potentially affect both stages of the bubble's lifespan. However, little is known about the wave effects over bubble growth phase. In the present work, this subject is investigated using a numerical single-bubble mechanical/solute transport model, which quantifies the effects of different parameters (amplitude and period) of the wave loading and of the water depth, over the bubble growth pattern in sediments and its specific characteristics. It was found that bubbles induce early sediment fracturing in the presence of waves, attributed to the low overburden load appearing at wave troughs. Bubbles at shallow depth rapidly grow at wave troughs by inducing multiple intense fracturing events. However, this ability decreases with an increasing water depth because of a slower solute influx. In the presence of waves, bubbles mature in shorter time, whose contrast to the no wave case is controlled by the ratio of wave amplitude to equilibrium water depth. Due to the higher frequency of occurrence of wave troughs for shorter-period waves, bubble growth is accelerated compared with the case of longer-period waves. Overall, our modeling suggests that the fastest bubble growth can be predicted for higher amplitude, short-period waves traveling in shallow water. We further infer that accelerated bubble growth, along with subsequent wave-induced ascent can sufficiently shorten the bubble's total lifespan in sediment, which explains the observed episodic *in situ* ebullitions correlated with wind- or storm-induced waves.

Keywords: methane bubbles, gassy sediment, muddy sediment, bubble growth, sediment fracturing, fracture mechanics, modeling

OPEN ACCESS

Edited by:
Michel Michaelovitch Mahiques, University of São Paulo, Brazil

Reviewed by:
Bernhard Wehrli, ETH Zürich, Switzerland
Victor Mikhailovich Stepanenko, Lomonosov Moscow State University, Russia

****Correspondence:***
Regina Katsman
rkatsman@univ.haifa.ac.il

Specialty section:
This article was submitted to Marine Geoscience, a section of the journal Frontiers in Earth Science

Received: *12 December 2021*
Accepted: *21 January 2022*
Published: *17 March 2022*

Citation:
Painuly A and Katsman R (2022) Mechanism of Faster CH_4 Bubble Growth Under Surface Waves in Muddy Aquatic Sediments: Effects of Wave Amplitude, Period, and Water Depth. Front. Earth Sci. 10:833918. doi: 10.3389/feart.2022.833918

INTRODUCTION

Formation of methane (CH_4) bubbles in shallow aquatic sediments is a widespread phenomenon (Bastviken et al., 2011), which is usually associated with synthesis of CH_4 during microbial remineralization of organic matter. Fine-grained cohesive (muddy) aquatic sediments develop discrete diffusion-fed bubbles (markedly larger than pore scale; Wheeler, 1988; Anderson et al., 1998), which elastically deform the sediment matrix and grow by fracturing (Abegg and Anderson, 1997; Johnson et al., 2002; Van Kesteren and van Kessel, 2002; Best et al., 2004; Boudreau et al., 2005; Reed et al., 2005; Jain and Juanes, 2009; Boudreau, 2012; Katsman et al., 2013). They rise in the sediment toward the water column due to buoyancy forces (Wheeler, 1990; Van Kesteren and van Kessel, 2002; Boudreau et al., 2005; Algar et al., 2011a; Algar et al., 2011b; Boudreau, 2012; Sirhan et al., 2019). Within aquatic environments, their entire life cycle is a matter of a great concern, due to the significant contribution of shallow aquatic sites to the global atmospheric CH_4 budget (USEPA, 2010; Saunois et al., 2016), and the bubbles ability to alter effective properties of gassy sediments—compressibility (Nageswaran, 1983; Sills and Wheeler, 1992) and undrained shear strength (Sills et al., 1991; Sills and Wheeler, 1992), which may induce slope failure in aquatic environments (Esrig and Kirby, 1977; Hovland et al., 2002; Bünz et al., 2005; Best et al., 2006).

The life cycle of a bubble within the sediment includes two subsequent stages: 1) bubble growth from its nucleation to mature size and configuration (with a closed tail, just prior to its ascent) (Abegg and Anderson, 1997; Johnson et al., 2002; Van Kesteren and van Kessel, 2002; Best et al., 2004; Reed et al., 2005; Barry et al., 2010; Katsman et al., 2013); and 2) subsequent rise of mature bubble from its place of nucleation toward the sediment - water interface (Wheeler, 1990; Van Kessel and Van Kesteren, 2002; Van Kesteren and van Kessel, 2002; Haeckel et al., 2004; Shin and Santamarina, 2010; Algar et al., 2011a; Algar et al., 2011b; Boudreau, 2012; Sirhan et al., 2019). Both of these stages within the sediment layers are governed by a complex interplay between geochemical properties of the ambient pore fluids (Martens and Klump, 1980; Abegg and Anderson, 1997) and the mechanical properties (fracture toughness, Young's modulus, and Poisson's ratio) of the sediment (Johnson et al., 2002; Algar and Boudreau, 2010; Boudreau, 2012; Katsman, 2015).

In addition, aquatic sediments often experience fluctuating loads, produced, for instance, by surface waves due to winds or storms, by swells or tides, and seasonal water level changes. Bubbles react to the mechanical energy of the varying hydrostatic load by rectifying their sizes and adjusting inner pressure, in accordance with the fluctuating overburden load. This is coupled with the process of CH_4 diffusion to a growing bubble from within the ambient sediments, responsible for bubble growth (Algar and Boudreau, 2009). Field studies often discern a correlation between episodic ebullition from aquatic sediments with variations in hydrostatic pressure (Martens and Klump, 1980; Miller and Oremland, 1988; Chanton et al., 1989; Mattson and Likens, 1990; Keller and Stallard, 1994; Scandella et al., 2011; Chen and Slater, 2016; Scandella et al., 2016; Chen et al., 2017), which was also recently confirmed by lab observations (Scandella et al., 2017) and numerical studies (Algar et al., 2011b; Katsman, 2019).

However, despite its importance, little is known about the effects of varying wave loading over the bubble growth phase, i.e., from its nucleation to mature configuration at the start of its ascent. A strong coupling between the net solute transport from the ambient sediment to the growing bubble with fluctuating size, along with difficulties in precise measuring and assessing bubble growth rates due to mud opacity, make it extremely complicated to explore this process *in situ* and to define its controls in aquatic sediments. Only a few studies based on numerical modeling quantified bubble growth under periodic wave loadings in muddy aquatic sediments (e.g., Boudreau et al., 2001; Algar and Boudreau, 2009; Algar et al., 2011b). These studies focused on bubble growth under a semidiurnal tidal loading (wave periods of 12 h) and its effect on processes of rectified diffusion and solute transport (due to pressure oscillations) to the growing bubble. The rectified diffusion was suggested to become important as $(\Delta P/P)^2 \rightarrow 1$, where ΔP is magnitude of wave induced load fluctuation, and P is the overburden load of the water column. The magnitude of $(\Delta P/P)^2$ is on the order of 0.0001–0.001 in the usual wind-induced waves (Boudreau et al., 2001) and can be up to ~0.05 in tides (Algar and Boudreau, 2009; Algar et al., 2011b). Due to a substantially lower magnitude of $(\Delta P/P)^2$ and the low frequency of oscillations of tides during the entire bubble growth period (about a week, Algar et al., 2011b), waves' contribution to bubble volume growth was suggested to be marginal (Boudreau et al., 2001; Algar and Boudreau, 2009; Algar et al., 2011b). However, due to the high surface area-to-volume ratio (an indicator of bubble's sensitivity to ambient solute field) of the thin sub-vertical bubbles growing in muds by fracturing, tidal actions could roughly contribute seven times more to bubble volume growth, compared with spherical bubbles of the equivalent volume (Algar and Boudreau, 2009). Nevertheless, an overall consistent quantification of the wave loading effect on bubble growth dynamics is missing. Specifically, it is unclear how the wave characteristics (wave period and amplitude) and water depths affect a bubble's growth in aquatic muds, and which factors would dominate.

In the present study, an underlying general quantitative mechanistic pattern and specific features of bubble growth in aquatic sediments, prior to bubble's ascent, under the action of surface wave loadings, are explored. Bubble growth is simulated under distinct wave characteristics (wave amplitude and period) at various ambient water depths. Results indicate that under the wave action, the bubbles grow faster compared with the no wave case, especially at shallow water depths and under higher amplitude and shorter wave periods. This is attributed to an early appearance of sediment fracturing, and in some cases to intense and frequent fracturing events that appear at the wave trough. Our findings associate this mechanism of accelerated bubble growth with episodic ebullitions at various aquatic sites to be correlated with wind or storm-induced surface waves, which is important in the context of a long-persisting uncertainty related to net CH_4 fluxes from shallow aquatic sediments.

MATERIALS AND METHODS

To analyze the effects of wave-induced periodic loadings on CH_4 bubble growth within muddy sediment, we used a coupled mechanical/solute transport numerical model, previously developed in Katsman et al. (2013) and Katsman (2015). This single-bubble model is applicable to fine-grained cohesive (muddy) sediments, where a bubble grows by a crack propagation within the framework of linear elastic fracture mechanics (LEFM) (e.g., Johnson et al., 2002; Boudreau et al., 2005; Best et al., 2006; Barry et al., 2010; Boudreau, 2012). The model simulates the coupled process of diffusion-driven bubble expansion due to a concentration gradient of dissolved CH_4 at the bubble surface, and the sediment's elastic-fracture mechanical response (Broek, 1982; Lawn, 1993; Gross and Seelig, 2017) to bubble growth. The modeling setup (**Figure 1A**) includes a small penny-shaped bubble seed with dimensions larger than a pore scale, embedded at the symmetry plane of a 3D sediment cell. The bubble's (crack's) spatial opening implicitly depends upon the inner bubble pressure, which continuously mounts due to an uninterrupted solute supply from the ambient sediment. This causes the bubble to grow elastically and gain stress intensity factor (Mode I SIF, K_I, a measure of the stress state at the crack front characterized by deformations normal to the crack surfaces; Broek, 1982; Lawn, 1993; Gross and Seelig, 2017). As such, K_I at each point of the crack front, F (**Figure 1A**), is evaluated employing a one-point methodology, using displacements at point P prescribed on the crack surface in the vicinity of point F (Citarella and Cricrì, 2010; Katsman et al., 2013):

$$K_I = \frac{E}{4(1-\nu^2)}\sqrt{\frac{\pi}{2d}}2w_n^P, \tag{1}$$

where ν is the Poisson's ratio, E is the Young's modulus, d is the distance between the points (**Figure 1A**), and w_n^P is a normal displacement of the crack surface at point P. As per the principles of LEFM, when the maximum value of SIF, K_I, over the front exceeds the sediment's Mode I fracture toughness, K_{IC} (a material parameter quantifying the sediment's crack resisting ability; Lawn, 1993; Gross and Seelig, 2017), the bubble (crack) initiates discrete differential fracturing along the front. Notably, the SIF along bubble front is always maximum at bubble's head (point B, **Figure 1A**; denoted here by K_{head}), since gravity-dependent compressive stress component in the ambient sediment produces a maximum opening there (Katsman et al., 2013; Katsman, 2015). Therefore, maximum crack increment always occurs at the buoyant bubble head (point B, **Figure 1A**) and decreases toward its tail (point A, **Figure 1A**) (Katsman et al., 2013). With an increase in the bubble's vertical height, the differences between local compressive stresses within the sediment at its head and tail increase (due to their dependence on gravity; Katsman, 2015); ultimately resulting in closure of the bubble's tail (i.e., zero openings), as an indicator of its mature configuration prior to its ascent. The model equations and input parameters used in simulations are listed in **Supplementary Tables S1** and **S2**, described in detail in Katsman et al. (2013) and Katsman (2015).

Under the action of surface waves, the effective water column height (H_{eff}) pulsates around its mean level (H_{eq}), approximated here as:

$$H_{eff} = H_{eq} + A\sin\left(\frac{2\pi t}{T}\right) \tag{2}$$

where A is the amplitude, T is the period of pulsation of the surface wave, and t is the time. A corresponding effective overburden load, σ_z^0, is described here as the sum of pulsating hydrostatic pressure of the water column (σ_H), and the permanent lithostatic pressure of the overlying sediment layer (σ_L), i.e., $\sigma_z^0 = \sigma_H + \sigma_L$. Here, $\sigma_L = \rho_s g H_s$, and $\sigma_H = \rho_w g H_{eff}$ (ρ_s, ρ_w are bulk sediment and water densities, g is gravity acceleration, and H_s is the thickness of the sediment layer overlying the modeled computation domain, **Figure 1A**).

For clarity of further analysis, the periodic oscillations in the effective overburden load (σ_z^0) produced by propagation of surface waves, can be differentiated in two subsequent loading phases: 1) "*unloading" phase 1*, described as the continuous fall of the overburden load, σ_z^0 (σ_z^{max} to σ_z^{min}), in response to a declining water level; and 2) *"loading" phase 2*, attributed to a continuous rise of the overburden load (σ_z^{min} to σ_z^{max}). A schematic illustration of the fluctuations in σ_z^0, induced by a surface wave having an amplitude of 0.22 m (A) and a time period of 3 s (T) over sediment submerged under 18 m of water (H_{eq}), is presented in **Figure 1B**.

Simulations are initiated with a small penny-shaped bubble having a radius of 4 mm (**Figure 1A**) and continue until the bubble attains mature size and configuration with closed tail (Katsman et al., 2013). This time period is specified as "Bubble maturity time" designated by t_m. Numerical simulations are performed at distinct ambient water column heights (H_{eq}, presented in subsection *Effect of the water depth on bubble growth*), and with distinct surface wave characteristics (A, T, presented in subsections *Role of ratio of wave amplitude to water depth over bubble growth* and *Role of wave periods over bubble growth*). Input conditions related to these characteristics used in simulations are summarized in **Table 1**. The model was designed within the COMSOL Multiphysics simulation environment, v.5.5.

RESULTS

Pattern of Bubble Growth Under the Wave Loading

First, we explore the general pattern and specific features of bubble growth under the wave action. In parallel and for comparison, bubble growth is simulated in the absence and presence of wave loadings, with conditions summarized in **Table 1** (runs 1, 2, respectively). Corresponding results of evolution of Mode I stress intensity factor at the bubble head, K_{head} (SIF at point B in **Figure 1A**), are demonstrated in **Figure 2**. In the absence of waves (run 1, green line), following the elastic expansion of the initial bubble cavity, K_{head} rises linearly (t = 0–10.95 s; see left inset of **Figure 2**), until K_{head} reaches the

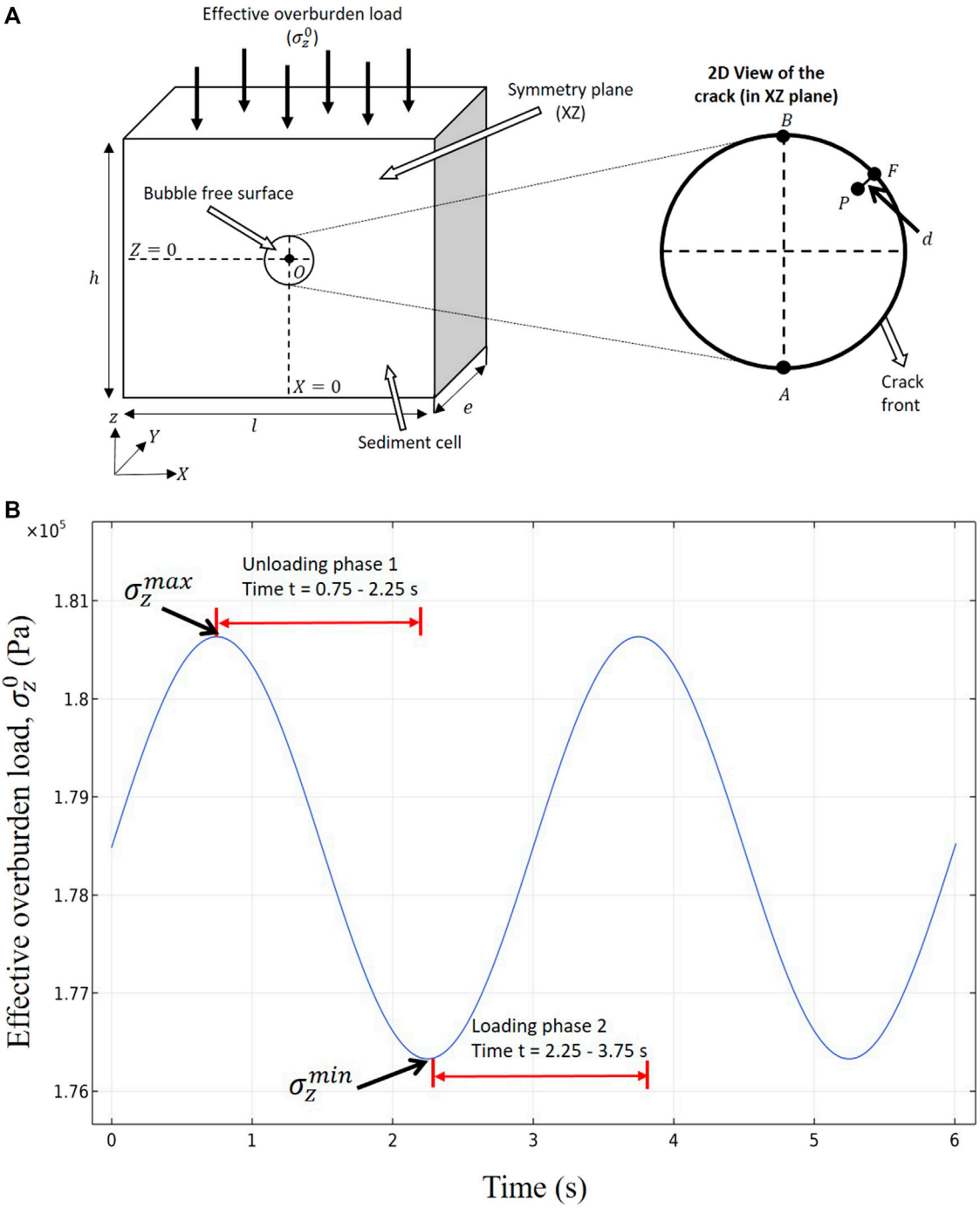

FIGURE 1 | Schematic illustration of modeling setup: **(A)** Computational domain consists of a 3D sediment box cut by a symmetry plane (XZ), with an embedded penny-shaped bubble seed (centered at origin, O). (X, Y, Z) depicts the global coordinate system. Top boundary of sediment is subjected to an effective overburden load, σ_z^0. Inset plot presents 2D in-plane view of penny-shaped (Mode I) crack surface and its front. Points A and B denote a bubble's tail and head, correspondingly. Point P on bubble surface (at fixed distance *d* from crack front) is specified to estimate the Stress Intensity Factor at the adjacent point F of the evolving bubble front. **(B)** Temporal evolution of effective overburden load (σ_z^0) over sediment submerged under 18-m water depth under surface waves of amplitude 0.22 m having a period of 3 s. In unloading phase 1 (t = 0.75–2.25 s, 3.75–5.25 s, etc.), the overburden load continuously decreases from its maximum (σ_z^{max}) to minimum (σ_z^{min}) value, and in loading phase 2 (t = 0–0.75 s, 2.25–3.75 s, and 5.25–6 s, etc.), the overburden load continuously rises from minimum (σ_z^{min}) to maximum (σ_z^{max}) value.

TABLE 1 | Input conditions used in simulations: to illustrate 1) a general pattern of bubble growth without and with (runs 1, 2) waves; 2) an effect of water depth (runs 3, 4) over the bubble growth; 3) an effect of wave amplitude-to-water depth ratio (runs 5, 6); and 4) an effect of wave periods (runs 7–10).

Run no	Mean water column height, H_{eq} (m)	Wave amplitude, A (m)	Wave period, T (s)	Wave amplitude-to-water column height ratio ($\bar{r} = A/H_{eq}$)	Bubble maturity time, t_m(s)	$\bar{t}^a$	Related figure
1	2	0	0	NA	391	NA	2, 3
2	2	0.22	3	0.11	353	9.71%	2, 3
3	18	0	0	NA	8,245	NA	4
4	18	0.22	3	0.012	7,976	3.2%	4
5	10	0	0	NA	2,897	NA	5
6	10	1.1	3	0.11	2,555	11.8%	5
7	2	0.22	10	0.11	357	8.6%	6
8	2	0.22	20	0.11	372	4.8%	6
9	2	0.22	30	0.11	377	3.5%	6
10	2	0.22	50	0.11	382	2.3%	6

[a]*Note: A contrast in time taken by bubbles to mature with and without wave loadings is measured (in percentage) as* $\bar{t} = 100 \cdot |t_m\,(no\ wave) - t_m\,(with\ wave)|/t_m\,(no\ wave)$.

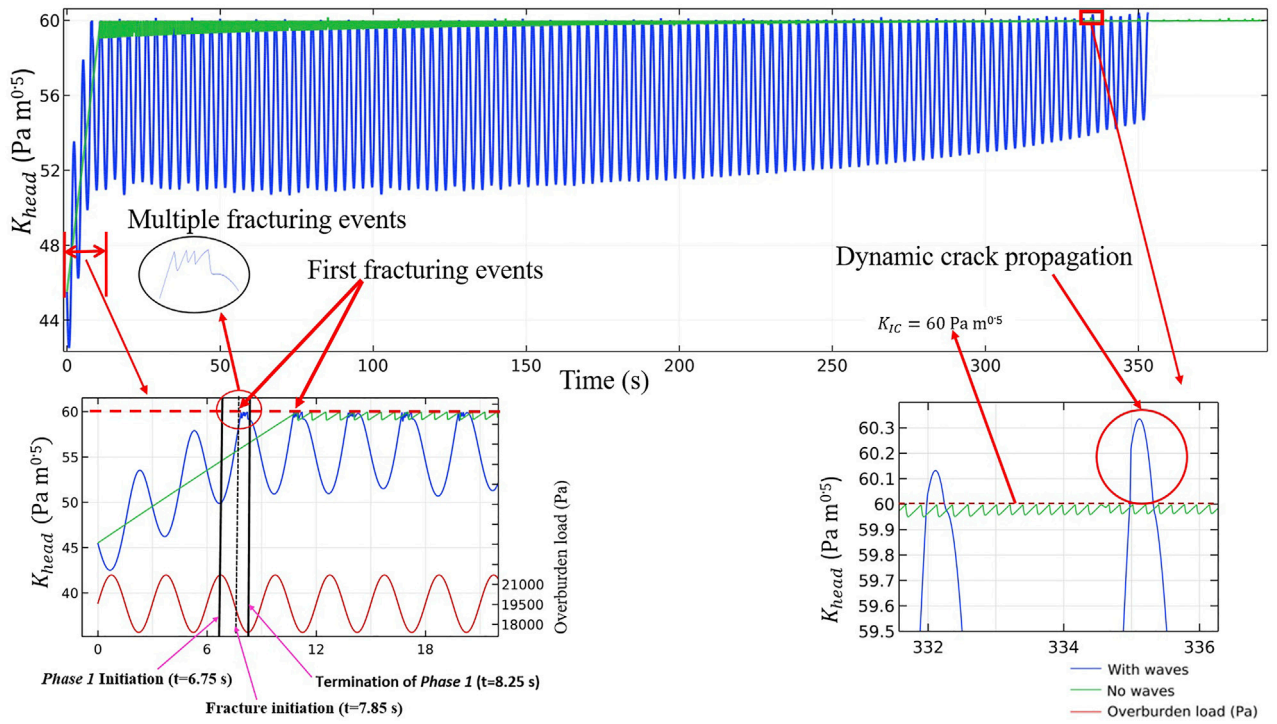

FIGURE 2 | The evolution of stress intensity factor at bubble head, K_{head}, for bubble growing in the presence (run 2, blue curve) and absence (run 1, green curve) of waves. Insets show the zoomed section of K_{head} profiles for t = 0–22 s (left inset) and t = 332 s–336 s (right inset). Left inset also depicts the corresponding oscillating overburden load, σ_z^0 (red curve, connected to the right axis). Under wave loadings, bubbles induce early fracturing (see first fracturing events marked in the left inset). K_{head} exhibits also periods of intense fracturing events (e.g., for t = 7.85 s–8.25 s, 10.75 s–11.25 s, etc.) at wave troughs and stages of temporarily ceased fracturing (e.g., for t = 8.25 s–10.75 s, 11.25 s–13.7 s, etc.). Stable saw tooth fracturing under the waves is produced at t = 0–~300 s; however, at later stages, bubble grows by temporarily inducing a dynamic fracturing (~t >300 s), where K_{head} exceeds K_{IC}. However, in contrast, under no wave conditions (run 1), K_{head} profile exhibits a continuous stable fracturing only (see left inset).

sediment's fracture toughness, K_{IC} (60 Pa m$^{1/2}$). At this time fracturing initiates, which in-turn results in a sharp drop in K_{head} (at t = 10.95 s; see left inset of **Figure 2**). With the continuous solute supply from the ambient sediment, this yields a repeated pattern of elastic expansion and sediment fracturing, thus, generating a saw-tooth-like K_{head} profile (**Figure 2**; observed also in other studies such as in Johnson et al., 2002; Algar and Boudreau, 2009; Boudreau, 2012; Katsman et al., 2013).

In contrast, in the presence of waves, the stress intensity factor at the bubble head (K_{head}) (**Figure 2**, blue line, run 2) oscillates around the corresponding values of K_{head} attained by the bubble at the elastic expansion stage under no-wave

conditions (left inset of **Figure 2**). Under the wave actions, there are two specific fracturing features that make this different from the fracturing pattern in the absence of wave loadings:

1. Early fracture initiation due to decline in σ_z^0 in the unloading stage (phase 1, **Figure 1B**).
2. Intense multiple fracturing events in the unloading stage (phase 1) near the wave trough.

Early fracturing appearance due to a σ_z^0 decline in the unloading stage (phase 1): Due to the wave action, fluctuations of $\sim\pm 4\ \mathrm{Pa\ m^{1/2}}$ in K_{head} are observed compared with corresponding values of K_{head} in the no wave case (**Figure 2**). Essentially, K_{head} is reversely synchronized to the oscillating effective overburden load, σ_z^0, in the presence of waves (red line in the left inset of **Figure 2**). Therefore, waves aid in achieving the fracturing condition ($K_{head} \geq K_{IC}$) a bit earlier, in comparison with a bubble grown in the absence of waves, due to the declining σ_z^0 in the unloading stage (phase 1 in **Figure 1B**, see a detailed explanation on this issue in **Supplementary Text S1**). Specifically, due to wave loading, the first fracturing event is observed at t = 7.85 s (see black dashed line in the left inset of **Figure 2**), in contrast to t = 10.95 s in the absence of waves (left inset in **Figure 2**).

Intense multiple fracturing events in the unloading stage (phase 1) near wave trough: Under the action of wave loadings, the K_{head} profile exhibits sequences of temporarily ceased fracturing events, with termination of the unloading phase 1 near wave troughs (e.g., between t = 8.25–10.75 s and 11.25–13.7 s, etc.; **Figure 2**), in contrast to the no wave case where fracturing continuously persists after its start (green profile, **Figure 2**). The fracturing temporally halts at the beginning of loading phase 2 (**Figure 1B**) because of the reduction in the bubble openings and, hence, in K_{head} (see **Eq. 1** and **Supplementary Text S1**), despite the continuous solute supply to the bubble. As waves decrease the overburden load near their troughs (red solid line, i.e., $\sigma_z^0 \rightarrow \sigma_z^{min}$), fracturing events re-appear (for example, between t = 7.85–8.25 s and 10.75–11.25 s, etc.; see left inset of **Figure 2**). Therefore, when the wave approaches its trough (i.e., $\sigma_z^0 \rightarrow \sigma_z^{min}$, red solid line), and fracturing re-initiates again, the bubble rapidly increases in size by more frequent and intense fracturing events compared with the no wave case. This rapid crack propagation at the wave troughs is due to the continuous piling-up of solute at the preceding wave loading stage. In simulation, this crack growth is manifested by two fracturing mechanisms (see two inset plots of **Figure 2**): 1) occurrence of multiple fracturing events in a stable fracturing regime (i.e., when K_{head} remains below K_{IC}, for time ~0–300 s, left inset); 2) bubble growth by dynamic fracture propagation (i.e., when despite the fracturing events, K_{head} temporarily rises higher than K_{IC}, at wave troughs, at a more advanced stage, ~t >300 s, applicable for a large bubble, right inset). Both stable and dynamic fracturing scenarios cease with initiation of loading phase 2, bringing K_{head} below K_{IC}.

As a result of the appearance of these early and multiple fracturing features, the bubble in run 2 earlier attains a larger surface area (e.g., between t = 7.85 and 10.95 s, **Figure 2**) and thus, grows with a higher total diffusive flux over its surface as compared with the bubble growing under no waves in run 1 (**Figure 3**). Therefore, bubbles growing under the wave action are able to mature in less time (t_m = 353 s) compared with bubbles growing under no waves (t_m = 391 s), **Table 1**.

Effect of the Water Depth on Bubble Growth

To explicitly demonstrate the effect of water depth on bubble maturity time, t_m, and fracturing pattern, we simulate bubble growth in sediment under a water depth of 18 m (without and with waves, runs 3 and 4, respectively, **Table 1**) and compare the results with those from run 2 simulated with the same wave amplitude and period. It can be seen from **Figure 4**, where evolution of K_{head} for runs 3, and 4 are shown, that bubbles do induce early fracturing (first fracturing at t = 80.75 s in the presence of waves and at t = 92.17 s in the absence of waves), but no multiple fracturing is observed. This is attributed to low diffusive flux of orders of 10^{-13} to $1.9 \cdot 10^{-12}$ kg/s for bubbles at water depth 18 m (run 3, 4) in contrast to $3.04 \cdot 10^{-13}$ to $4.02 \cdot 10^{-12}$ kg/s at 2 m water depth in run 2, over the entire bubble growth period, as explained below.

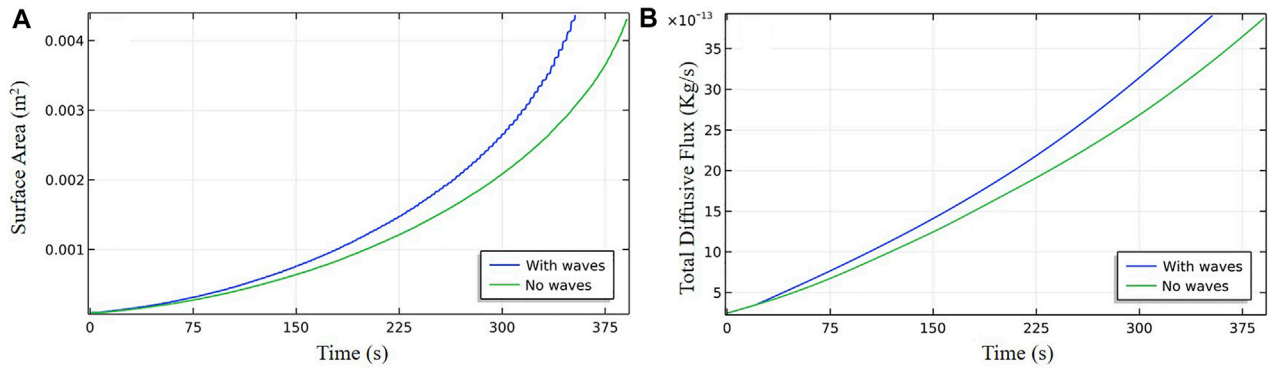

FIGURE 3 | Temporal growth of surface area [panel **(A)**] and total diffusive flux [panel **(B)**] for bubbles growing in sediment under a 2 m water depth, in the presence (run 2, blue curve) and absence (run 1, green curve) of waves. Attributed to early and multiple fracturing, bubbles growing in the presence of waves gain surface area and total diffusive flux comparatively faster, thus, maturing in less time (t_m = 353 s, 391 s in the presence and the absence of waves, respectively).

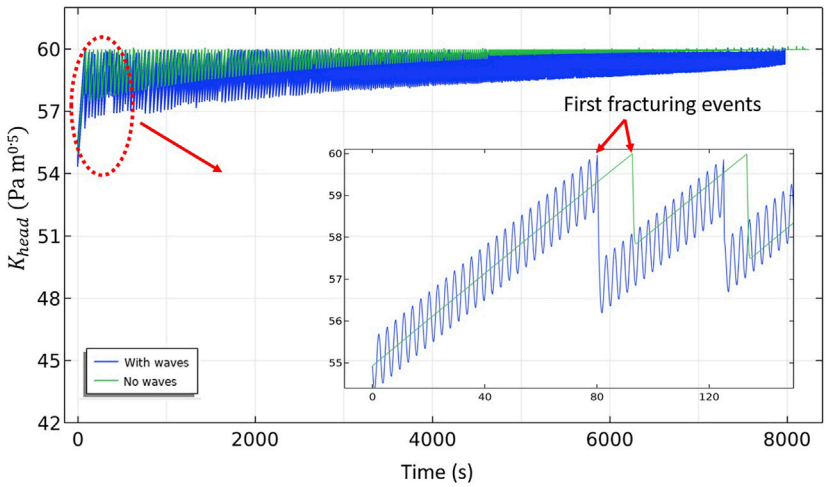

FIGURE 4 | Evolution of K_{head} for bubbles from run 3 and run 4, presented to quantify an effect of water column height. Inset plot presents a zoomed section of K_{head} profile for time interval t = 0–140 s. In the presence of waves (run 4, blue curve), K_{head} fluctuates around the corresponding mean value from the no-wave case (run 3, green curve) and induces first fracturing at 80.07 s in contrast to first fracturing at t = 92.17 s in the absence of waves. Attributed to higher overburden load (of 18 m water column), and hence, lower total solute flux, a bubble is not able to induce multiple fracturing at wave troughs (see text for detailed explanations).

Bubbles in deeper water (i.e., under the higher overburden load, σ_z^0) grow with higher inner pressure, P_b (Eq. 15 in Katsman, 2015). This, in turn, increases the solute concentration at the bubble surface (**Supplementary Equation S6** in **Supplementary Material**) and, thus, reduces the temporal total diffusive flux to the growing bubble (**Supplementary Equation S3** in **Supplementary Material**). Therefore, the CH_4 flux supplied to the growing bubble, and thus, the gaseous CH_4 accumulated in the bubble per wave period, naturally decreases with an increase in the water depth. Consequently, after a first fracturing event, the amount of solute required to induce the next fracturing event may accumulate over a substantially large number of wave periods (e.g., see inset of **Figure 4** between t = 80 and 125 s; attributed to a slower bubble influx). Hence, deeper water decreases the potential to induce multiple fracturing events near the wave trough (as is observed in the shallow depth of run 2, **Figure 2**).

Therefore, in sediments submerged under shallow water depths (as modeled in run 2), bubbles incur early fracturing as well as induce multiple fracturing events (as described in **Figure 2**) near the wave troughs, sometimes supplemented by a dynamic fracturing regime at a later stage of the bubble growth, which expedites bubble growth (**Figure 2**). Therefore, a bubble under 2 m of water was able to mature in nearly ~9.71% ($\bar{t}$) less time compared with a bubble in the absence of waves (run 1, 2; **Table 1**). Additionally, simulation in shallower water at a depth of 0.5 m (not shown here) under the same wave conditions as in runs 2, 4, indicated a ~30% decrease in bubble maturity time (see **Supplementary Table S3** in **Supplementary Material**). However, a bubble's ability to induce multiple fracturing under a wave trough distinctively decreases with increasing water column height, as indicated above. Thus, the bubble in run 4 with 18 m water column height could only grow nearly ~3.2% ($\bar{t}$) faster compared with the bubble in the absence of waves, run 3 (the maturity time, t_m, is 7,976 and 8,245 s, correspondingly). This indicates that the effectiveness of wave loadings to expedite bubble growth decreases with increasing water column height (for constant A, T).

Role of Ratio of Wave Amplitude to Water Depth Over Bubble Growth

To further explore the role of the ratio of wave amplitude to water depth ($\bar{r} = A/H_{eq}$), over the bubble maturity time, t_m, we analyze results of bubble growth from runs 5, 6 (**Table 1**) and compare their maturity times with those from run 2. Ambient water column height and wave characteristics in runs 5, 6 were chosen in a way to preserve a constant ratio, $\bar{r}$ = 0.11, as in run 2.

The magnitude of fluctuations in K_{head} in runs 2 and 6 is approximately the same, i.e., ~ ±4 Pa m$^{1/2}$ (left inset of **Figure 2** and inset of **Figure 5**), and is attributed to the same values of the ratio, $\bar{r}$. Therefore, in run 6, at each wave trough, K_{head} is effectively enhanced by ~4 Pa m$^{1/2}$, compared with the mean value of K_{head} in the no wave case (runs 6 and 5, respectively; **Figure 5**). This enables bubbles to induce early fracturing at t = 74.25 s in the presence of waves (run 6), compared with t = 115.2 s under no wave conditions (run 5). By incurring early fracturing events due to wave loadings, a bubble under a 10 m water column is able to attain maturity in 2,555 s (run 6), while in the absence of waves the bubble takes 2,897 s to mature (run 5). Despite distinct overburden loads, the contrast in bubble maturity time in runs 2 and 6 is quite similar (at water depths of 2, and 10 m, bubble maturity time is reduced by nearly 9.71% and 11.8% ($\bar{t}$), respectively, under the same $\bar{r}$).

Furthermore, following **Eq. 2**, the rate of change in scaled hydrostatic overburden load ($\sigma_H^s = \sigma_{eff}/\sigma_{eq}$, where $\sigma_{eff} = \rho_w g H_{eff}$ and $\sigma_{eq} = \rho_w g H_{eq}$) induced by waves is given as:

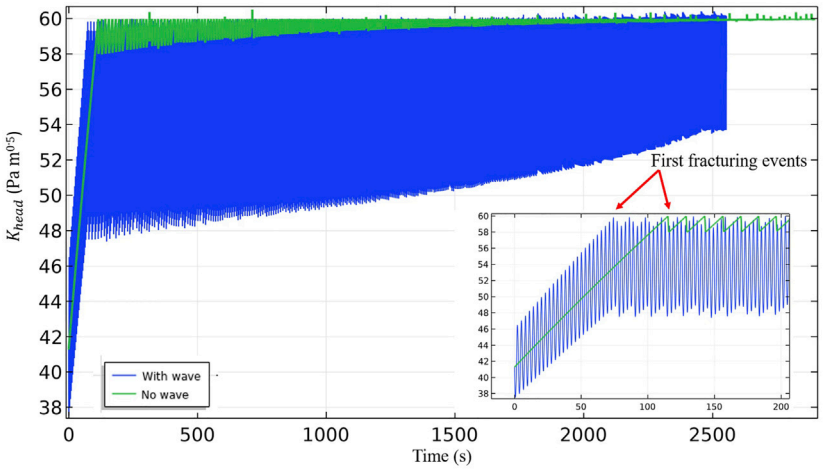

FIGURE 5 | Evolution of K_{head} for bubbles from runs 5 (without wave loading, green curve), 6 (with wave loading, blue curve) focused on wave amplitude to water depth ratio verification. Zoomed section of K_{head} profile for time interval t = 0–200 s is presented in inset. Under action of waves of amplitude 1.1 m, K_{head} fluctuates about ±4 Pa m$^{1/2}$ around corresponding mean values of K_{head} in the absence of wave loadings. At each wave trough, a bubble's K_{head} is effectively enhanced by ~4 Pa m$^{1/2}$, enabling the bubble to attain first fracturing event earlier, at t = 74.25 s in the presence of wave, while at t = 115.2 s in the absence of waves.

$$\frac{\partial(\sigma_H^s)}{\partial t} = \bar{r} \cdot \cos\left(\frac{2\pi t}{T}\right) \cdot \frac{2\pi}{T} \tag{3}$$

where H_{eff}, H_{eq} are the effective and the equilibrium water column heights (as given by **Eq. 2**), respectively. The horizontal load at the bubble surface (σ_y) is related to vertical overburden load (σ_{eff}) by the relation $\sigma_y = \frac{\nu}{1-\nu} \cdot \sigma_{eff}$, where ν is Poisson's ratio (under the uniaxial (vertical) strain boundary condition, as prescribed in the present model, Katsman et al., 2013; Katsman 2015). For same time period values, T, **Eq. 3** suggests that the rate of change in σ_H^s and, thus, in σ_y, explicitly depends upon the ratio of wave amplitude to water depth, $\bar{r}$. As a result, this generates oscillations of equivalent magnitude in bubble openings (w_n, **Supplementary Equation S10**) and, hence, in K_{head}, in bubbles growing in environments with similar ratios, $\bar{r}$.

Notably, as attributed to increased water depths, the total solute flux to bubble in run 6 (of orders of ~$20 \cdot 10^{-13}$ kg/s at mature configuration) is smaller compared with that in run 2 (of orders of ~$40 \cdot 10^{-13}$ kg/s at the corresponding mature configuration; **Figure 3B**), and hence, their maturity time t_m is different (2,555 s and 353 s, respectively). Therefore, a similarity, in contrast to relative times taken by bubbles to mature with and without wave loadings, $\bar{t}$, should be attributed to $\bar{r}$. However, in run 2, bubble growth is enhanced due to the appearance of multiple fracturing (**Figure 2**) affected by an efficient solute influx. In contrast, in run 6, the growth is swift compared with the corresponding bubble in run 5, due to longer duration of early fracturing affected by a high $\bar{r}$ value, while the bubble in run 5, under no waves, still experiences an elastic expansion stage caused by the slow solute influx. Finally, to achieve the same values of ratio $\bar{r}$ in deep waters, high-amplitude waves would be a prerequisite to significantly expedite the bubble growth.

Role of Wave Periods Over Bubble Growth

In order to understand the effect of wave periods (T) over bubble growth, we simulate bubble growth under fixed water column height (H_{eq} = 2 m) and with constant wave amplitudes (A = 0.22 m) (as in run 2), but with different wave periods, T (runs 7 to 10, **Table 1**). A comparison between bubble maturity times (t_m) for runs 2 (T = 3 s), 7 (T = 10 s), 8 (T = 20 s), 9 (T = 30 s), and 10 (T = 50 s) with that in the no wave case (run 1) is presented in **Figure 6**.

Simulations reveal that smaller period waves expedite bubble growth (**Figure 6**): for instance, a bubble matures in 353 s when T = 3 s (run 2), compared with 382 s when T = 50 s (run 10). For smaller wave periods, the bubble is exposed to wave trough loadings (i.e., low overburden load) more frequently, over the entire period of its growth. Thus, bubble growth via early and/or multiple fracturing events occurs more frequently in the presence of short period waves. This facilitates bubbles attaining mature size in less time, as seen in **Figure 6**.

DISCUSSION

Our calculations assert that surface waves developed in the water column with the passage of winds or storms, reduce the duration of the growth phase of bubbles, and thus allow early upward buoyant bubble rise. For instance, the water depth and surface wave characteristics simulated in runs 1 and 2 (**Table 1**) may be associated with the usual ambient conditions in the shallow littoral zone of Lake Constance, Europe, in the presence of synoptic scale winds from the southwest-west and northeast (Appt et al., 2004; Hofmann et al., 2008). The data in runs 3 and 4 agree with ambient conditions at the 18 m isobaths of Lake Kinneret, Israel, in the presence of Mediterranean summer sea breezes (Serruya, 1975; Zohary et al., 2014). There is a reduction of ~9% and 3% in the time duration of the bubble growth period

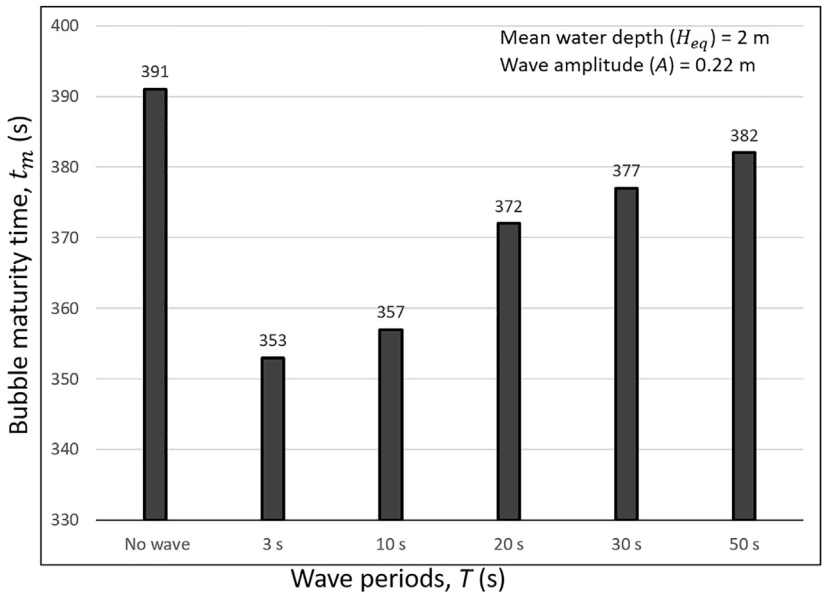

FIGURE 6 | Maturity time, t_m, of bubbles growing under a 2 m-deep water under wave amplitude (A = 0.22 m), with different wave periods, T = 3, 10, 20, 30, 50 s, and under no waves. Under shorter period waves, a bubble matures in comparatively less time (see text for detailed explanations).

at the respective sites in the presence of the surface waves under the modeled conditions.

In shallow water sites (e.g., under water depth 2 m, run 2), at the stage when bubbles gain sufficiently large heights, they are able to grow by inducing a dynamic fracturing style at each wave trough (right inset of **Figure 2**). This agrees with the principles of LEFM (Broek, 1982; Lawn, 1993; Gross and Seelig, 2017; Sirhan et al., 2019), which assert that a crack grows dynamically (runs unrestrictedly) when mechanical energy dissipated per unit crack increment exceeds the energy required to create new crack surfaces (Lawn, 1993). In our simulation (run 2), the dynamic crack propagation appeared when the crack's vertical height and total size grew beyond a critical limit (see Sirhan et al., 2019, for details). Such bubbles can unrestrictedly proceed from a dynamic growth stage to a dynamic ascent toward the sediment–water interface and can potentially escape from the sediment (Sirhan et al., 2019), if the wave action halts. Quantifying these processes provides a valuable insight into understanding the observed correlation between winds and enhanced gas effluxes at various sites with microbially mediated CH_4 (Miller and Oremland, 1988; Mattson and Likens, 1990; Keller and Stallard, 1994). For example, at Lake Gatun (Panama) average winds of 4–7 $m\,s^{-1}$ appear to enhance gas fluxes up to ~500 $ml\,m^{-2}\,h^{-1}$. This is about ~20 $ml\,m^{-2}\,h^{-1}$ under no wind conditions (in 1.4–4.5 m water depth), ~98% of which occurred by bubbling (Keller and Stallard, 1994). A gas flux of ~500 $ml\,m^{-2}\,h^{-1}$ indicates liberation of nearly 24×10^3 mature bubbles per square meter of the lake surface per hour (assuming a volume of one mature bubble as $21 \times 10^{-9}\,m^3$, following the current model) and nearly 960 bubbles in the absence of winds (neglecting CH_4 bubble volume loss in the oxidizing zone, which is negligible for rapidly rising bubbles in shallow waters, Katsman, 2019). The high contrast in the amount of the escaping bubbles indicates that they rapidly grow in size, gain maturity in the presence of waves, and are effectively able to escape the sediments. Also, the continuous persistence of intensive bubbling up to 4–6 h (Keller and Stallard, 1994) is indirect evidence of the accelerated permanent bubbles growth that ultimately reach their maturity sizes under the waves. This is especially important for cases when bubble "no-growth" condition (Algar and Boudreau, 2010) occurs within the sediment under no waves, wherein the wave action may induce a persistent bubble growth.

Moreover, intense ebullition in the presence of surface waves can be attributed to a dynamic ascent of mature bubbles, which are pulled out from their stationary positions at a gas horizon and propagate unrestrictedly toward the sediment–water interface (Katsman, 2019). In shallow water depths where wave height is comparable with the water column height (as in run S2, **Supplementary Table S3**), acceleration in bubble growth (prior to its ascent) is significant (~30% contrast in the maturity times) and can also significantly decrease the bubble lifespan. However, in other cases simulated in this study, it is smaller (~2%–12% contrast in the maturity times, **Table 1**) and contributes to the enhanced ebullition fluxes via the mechanisms discussed above.

Our results indicate that waves with large periods (for example, tides) would have a very marginal effect over the bubble maturity time (as indicated in **Figure 6**, runs 7–10), as was also suggested previously by Boudreau et al. (2001), Algar and Boudreau (2009), and Algar et al. (2011b). However, a correlation of gas emissions with falling tides observed at a cold seep offshore Vancouver Island, British Columbia, Canada, was attributed to a decreasing pressure on the sub-

bottom fluid system (Römer et al., 2016). According to our study, this should shorten the bubble growth period due to the enhanced solute transport (run 2 compared with run 4). Decreased CH_4 solubility under the decreasing tidal load can fairly enhance the bubble exsolution (Römer et al., 2016; Blouin et al., 2019).

Moreover, a long period of tidal loading could affect migration of mature bubbles toward the sediment–water interface. For example, Chanton et al. (1989) found at White Oak River estuary, North Carolina, that bubbles release from sediment were closely coupled with daily tidal activities. The rate of bubble liberation rate to the water column was found to increase significantly, when the water column declined from its highest to its lowest water level (at an ambient water depth of ~70 cm, wave amplitude ~20 cm; $\bar{r}$ ~0.285). Rising bubbles enhanced the gas flux from ~0.05 ml min^{-1} m^{-2} at a high tide to ~3 ml min^{-1} m^{-2} at a low tide (a release of respectively 12 and 144 bubbles min^{-1} m^{-2} at high and low tide, respectively; assuming a volume of one mature bubble as 21×10^{-9} m^3, following the current model). Such an enhanced ebullition can be attributed to release of bubbles from shallow gas horizons due to a decrease in overburden load at low tides (as suggested by Katsman, 2019).

Bubble growth in muds is linked to the available dissolved CH_4 concentration in the ambient sediment, which is site specific, depending on local CH_4 production rate (Martens and Klump, 1980; Abegg and Anderson, 1997; Liu et al., 2020), and also to the diffusion process, supplying solute to the bubble (see **Supplementary Equation S3**). This process is controlled by: 1) the concentration gradient of CH_4 at the bubble surface and the ambient dissolved CH_4 concentration in the pore waters; and 2) the tortuosity-corrected CH_4 diffusion coefficient in the bulk sediment. Under deeper waters, bubbles in mud grow by developing higher inner pressures, P_b (see Eq.15 in Katsman, 2015) and, hence, gain higher CH_4 concentrations at their surfaces (**Supplementary Equations S4 and S6**). This depletes the concentration gradient between the bubble surface and ambient sediment, slowing the overall growth rate of the bubble (as noticed in run 3 compared with runs 1 and 5, **Table 1**).

Ambient dissolved CH_4 concentrations in pore waters of shallow sediments is a result of a long term CH_4 production. Zero CH_4 local production rate (**Supplementary Equation S2**) is used in our simulations to avoid a permanent increase in concentrations within our small computational domain where no CH_4 consumption is prescribed. Identical CH_4 concentration boundary conditions are prescribed in all the simulations to allow a consistent comparison, associated with supersaturation under all the modeled overburden loads. In the natural settings, such quasi-steady state CH_4 concentrations (Adler et al., 2011) as those simulated in this study are produced by spatially separated CH_4 production and consumption zones under a small temporal variability in their rates that interchange the solute by diffusion (Martens and Berner, 1977). Modeling these more complex settings in a larger computational domain seem unnecessary for the bubble growth problem studied here in contrast to the bubble migration.

Additionally, the local production rates that rely on a variety of geochemical and environmental factors predefine the ambient CH_4 pore water concentrations and differ significantly between the environments (Zamanpour et al., 2020). Persistent fracture-driven bubble growth is also dependent on muddy sediment mechanical properties, suggesting that weaker sediments along with larger CH_4 production may significantly expedite bubble growth and induce its ebullition (Zamanpour et al., 2020). Wave action studied in this paper also contributes to this process.

Mud constitutes a mixture of clay- and silt-sized (<63 μm; NEN, 1989; Winterwerp and van Kesteren, 2004) particles. The hygroscopic properties of flat, small clay particles with large surface areas reduce the effective porosity and, thus, mobility of water content through the sediment's pore structure (Mitchell and Soga, 2005; Sevee, 2010). Therefore, the effective porosity of clayey muds can be much smaller than that of sandy sediment (see Sirhan et al., 2019 and references therein). It can be smaller than 20% of the effective porosity specified in the current paper (**Supplementary Table S2**). This will hamper the supply of dissolved CH_4 and will yield a slower diffusive flux to the growing bubble and, hence, slower bubble growth in muds (e.g., a week-long scale of a bubble's growth was suggested by Algar et al., 2011b). In this case, even the tides (with shorter periods than the bubble growth time scale) may expedite the bubble growth, by a more frequent exposure to the tide/wave trough loadings, according to our study.

Muddy *in situ* sediments can maintain partially annealed rise paths (Martens, 1976; Martens and Klump, 1980) formed by the upward migration of older bubbles, leading to the partial breakage of cohesive interparticle bonds (Algar et al., 2011b; Boudreau, 2012). After the initial bubbles leave the sediment, subsequent bubbles with smaller volumes may rise through these tracts, correlated with a temporal reduction in fracture toughness (Algar et al., 2011b) or tensile strength (Scandella et al., 2017) of these conduits or channels. Subsequent bubbles can have mean volumes as low as 1/200 compared with the initially rising bubble in intact sediment (Algar et al., 2011b). In the presence of wave loadings, not only the subsequent bubbles could grow faster, but the vertical conduits or channels through which they rise are also forced to dilate periodically (Scandella et al., 2011), in response to fluctuations in the effective overburden load; paving the way for their "easy" liberation into the water column (e.g., Martens and Klump, 1980; Scandella et al., 2011; Algar et al., 2011b; Scandella et al., 2017). This facilitates a "dynamic" bubble escape from the shallow gas horizon within the sediment under shorter-period waves of higher amplitude traveling in shallow water (Katsman, 2019), and explains the rise of multiple bubbles observed in the field in the presence of wind- or storm-induced surface waves (Martens, 1976; Martens and Klump, 1980; Mattson and Likens, 1990).

Natural lakes occasionally have regions with irregular bathymetry with significant depth changes, for instance, Lake Kinneret in Israel, with a maximum depth of ~40 m (Zohary et al., 2014). This enforces spatially distinct hydrostatic conditions over the lake (when the ratio, $\bar{r} = A/H_{eq}$, varies substantially due to the variability in H_{eq}). The present study suggests that in water bodies where organic matter is distributed mainly in littoral zones by river inflow (e.g., Lake Kariba in Zambia and Zimbabwe; Coche, 1974; DelSontro et al., 2011), wave loadings should contribute substantially to bubble growth (DelSontro et al., 2011) and, hence, enhance ebullition fluxes from those regions. Conversely, in aquatic sites where organic matter is concentrated in

profundal deeper zones, the slow bubble growth at CH_4-generating sites attributed to higher hydrostatic loading, could ultimately lead to the occurrence of stationary bubbles (or their slow growth over the large time scale) forming sub-surface gas horizons despite the wave action. For instance, major bubble formation is reported to occur in Kinneret sediments under the deeper waters, thus, resulting in higher gas content in the deepest zone of the lake (water depth >15 m; Uzhansky et al., 2020; Liu et al., 2020). This is attributed to refocusing of autochthonous organic matter generated during seasonal phytoplankton blooms (Zohary et al., 2014) by a complex hydrodynamic regime and lake stratification in these deep zones (Ostrovsky and Tęgowski, 2010).

There is a persistent uncertainty associated with atmospheric CH_4 contributed from shallow aquatic sediments (Kirschke et al., 2013). This is largely due to the heterogeneous spatiotemporal nature of bubble growth and migration in aquatic sediments. The current work is intended to better characterize the bubble growth in sediments subjected to periodic wave actions, which allows an evaluation of their connections to bubble emissions to the water column.

CONCLUSION

We demonstrate that periodic wave loading accelerates growth of bubbles incubated within cohesive fine-grained aquatic sediments. We analyze the specific mechanisms by means of which bubble growth is altered, compared with the calm water/no wave case. The following conclusions can be drawn:

1. Under shallow water depth, bubbles induce early as well as induce multiple fracturing under the troughs of waves passing overhead. At a later stage bubble growth can be supplemented by a dynamic fracturing regime that may contribute to initiation of unrestricted upward migration of bubbles in sediment. However, under deeper water, bubbles induce only early fracturing and no multiple fracturing from passage of wave troughs. Therefore, as the water depth increases, the effectivity of wave loadings to expedite bubble growth decreases.
2. Similar values of the wave amplitude to water depth ratio ($\bar{r} = A/H_{eq}$) induce similar rates of change in the scaled hydrostatic overburden load over sediments. Thus, the relative contrast in bubble maturity time in the presence and absence of waves, for aquatic sediments with similar $\bar{r}$, is similar.
3. With an increase in wave periods, the frequency of wave trough unloading (when early fracturing and/or multiple fracturing events occur) decreases over the entire time of bubble growth. Therefore, the time of bubble maturity increases with the increase in wave period.
4. Overall, our modeling suggests that the fastest bubble growth can be predicted when higher-amplitude short-period waves travel in shallow water (i.e., high $\bar{r}$ ratio and short wave period).

DATA AVAILABILITY STATEMENT

The original contributions presented in the study are included in the article/**Supplementary Material**, Further inquiries can be directed to the corresponding author.

AUTHOR CONTRIBUTIONS

Conceptualization, AP and RK; numerical computations, AP; result validation, RK; formal analysis, AP and RK; original draft preparation, AP; review and editing, funding acquisition and resources, RK. All authors have read and agreed to the published version of the manuscript.

FUNDING

This project was supported by the Israel Science Foundation, Grant No. 1441-14, by United States-Israel Binational Science Foundation, Grant No. 2018150, and by the Institutional Postdoctoral Fellowships from the University of Haifa, Israel.

ACKNOWLEDGMENTS

We would like to thank the Editor and two Reviewers for their contributions in enhancing this paper. Improvement of the text by Dr. John K. Hall is greatly appreciated.

SUPPLEMENTARY MATERIAL

The Supplementary Material for this article can be found online at: https://www.frontiersin.org/articles/10.3389/feart.2022.833918/full#supplementary-material

REFERENCES

Abegg, F., and Anderson, A. L. (1997). The Acoustic Turbid Layer in Muddy Sediments of Eckernföerde Bay, Western Baltic: Methane Concentration, Saturation and Bubble Characteristics. *Mar. Geology.* 137 (1-2), 137–147. doi:10.1016/S0025-3227(96)00084-9

Adler, M., Eckert, W., and Sivan, O. (2011). Quantifying Rates of Methanogenesis and Methanotrophy in Lake Kinneret Sediments (Israel) Using Pore-Water Profiles. *Limnol. Oceanogr.* 56 (4), 1525–1535. doi:10.4319/lo.2011.56.4.1525

Algar, C. K., Boudreau, B. P., and Barry, M. A. (2011a). Initial Rise of Bubbles in Cohesive Sediments by a Process of Viscoelastic Fracture. *J. Geophys. Res.* 116, B04207. doi:10.1029/2010JB008133

Algar, C. K., Boudreau, B. P., and Barry, M. A. (2011b). Release of Multiple Bubbles from Cohesive Sediments. *Geophys. Res. Lett.* 38, L08606. doi:10.1029/2011GL046870

Algar, C. K., and Boudreau, B. P. (2010). Stability of Bubbles in a Linear Elastic Medium: Implications for Bubble Growth in marine Sediments. *J. Geophys. Res.* 115, F03012. doi:10.1029/2009JF001312

Algar, C. K., and Boudreau, B. P. (2009). Transient Growth of an Isolated Bubble in Muddy, fine-grained Sediments. *Geochimica et Cosmochimica Acta* 73 (9), 2581–2591. doi:10.1016/j.gca.2009.02.008

Anderson, A. L., Abegg, F., Hawkins, J. A., Duncan, M. E., and Lyons, A. P. (1998). Bubble Populations and Acoustic Interaction with the Gassy Floor of Eckernförde Bay. *Continental Shelf Res.* 18 (14-15), 1807–1838. doi:10.1016/S0278-4343(98)00059-4

Appt, J., Imberger, J., and Kobus, H. (2004). Basin-scale Motion in Stratified Upper Lake Constance. *Limnol. Oceanogr.* 49 (4), 919–933. doi:10.4319/lo.2004.49.4.0919

Barry, M. A., Boudreau, B. P., Johnson, B. D., and Reed, A. H. (2010). First-order Description of the Mechanical Fracture Behavior of fine-grained Surficial marine Sediments during Gas Bubble Growth. *J. Geophys. Res.* 115, F04029. doi:10.1029/2010JF001833

Bastviken, D., Tranvik, L. J., Downing, J. A., Crill, P. M., and Enrich-Prast, A. (2011). Freshwater Methane Emissions Offset the continental Carbon Sink. *Science* 331 (6013), 50. doi:10.1126/science.1196808

Best, A. I., Richardson, M. D., Boudreau, B. P., Judd, A. G., Leifer, I., Lyons, A. P., et al. (2006). Shallow Seabed Methane Gas Could Pose Coastal hazard. *Eos Trans. AGU* 87 (22), 213–217. doi:10.1029/2006EO220001

Best, A. I., Tuffin, M. D. J., Dix, J. K., and Bull, J. M. (2004). Tidal Height and Frequency Dependence of Acoustic Velocity and Attenuation in Shallow Gassy marine Sediments. *J. Geophys. Res.* 109, B08101. doi:10.1029/2003JB002748

Blouin, A., Sultan, N., Callot, J.-P., and Imbert, P. (2019). Sediment Damage Caused by Gas Exsolution: A Key Mechanism for Mud Volcano Formation. *Eng. Geology.* 263, 105313. doi:10.1016/j.enggeo.2019.105313

Boudreau, B. P., Algar, C., Johnson, B. D., Croudace, I., Reed, A., Furukawa, Y., et al. (2005). Bubble Growth and Rise in Soft Sediments. *Geol* 33 (6), 517–520. doi:10.1130/G21259.1

Boudreau, B. P., Gardiner, B. S., and Johnson, B. D. (2001). Rate of Growth of Isolated Bubbles in Sediments with a Diagenetic Source of Methane. *Limnol. Oceanogr.* 46 (3), 616–622. doi:10.4319/lo.2001.46.3.0616

Boudreau, B. P. (2012). The Physics of Bubbles in Surficial, Soft, Cohesive Sediments. *Mar. Pet. Geology.* 38 (1), 1–18. doi:10.1016/j.marpetgeo.2012.07.002

Broek, D. (1982). *Elementary Engineering Fracture Mechanics*. 3rd ed. Boston, Mass: Kluwer Academic Publishers.

Bunz, S., Mienert, J., Bryn, P., and Berg, K. (2005). Fluid Flow Impact on Slope Failure from 3D Seismic Data: a Case Study in the Storegga Slide. *Basin Res.* 17 (1), 109–122. doi:10.1111/j.1365-2117.2005.00256.x

Chanton, J. P., Martens, C. S., and Kelley, C. A. (1989). Gas Transport from Methane-Saturated, Tidal Freshwater and Wetland Sediments. *Limnol. Oceanogr.* 34 (5), 807–819. doi:10.4319/lo.1989.34.5.0807

Chen, X., Schäfer, K. V. R., and Slater, L. (2017). Methane Emission through Ebullition from an Estuarine Mudflat: 2. Field Observations and Modeling of Occurrence Probability. *Water Resour. Res.* 53 (8), 6439–6453. doi:10.1002/2016WR019720

Chen, X., and Slater, L. (2016). Methane Emission through Ebullition from an Estuarine Mudflat: 1. A Conceptual Model to Explain Tidal Forcing Based on Effective Stress Changes. *Water Resour. Res.* 52 (6), 4469–4485. doi:10.1002/2015WR018058

Citarella, R., and Cricrì, G. (2010). Comparison of DBEM and FEM Crack Path Predictions in a Notched Shaft under Torsion. *Eng. Fracture Mech.* 77 (11), 1730–1749. doi:10.1016/j.engfracmech.2010.03.012

Coche, A. G. (1974). "Limnological Study of a Tropical Reservoir," in *Lake Kariba: A Man-Made Tropical Ecosystem in Central Africa*. Editors E. K. Balon and A. G. Coche (The Hague, Netherlands: Dr. W. Junk Publishers).

DelSontro, T., Kunz, M. J., Kempter, T., Wüest, A., Wehrli, B., and Senn, D. B. (2011). Spatial Heterogeneity of Methane Ebullition in a Large Tropical Reservoir. *Environ. Sci. Technol.* 45 (23), 9866–9873. doi:10.1021/es2005545

Esrig, M. I., and Kirby, R. C. (1977). Implications of Gas Content for Predicting the Stability of Submarine Slopes. *Mar. Geotechnology* 2 (1-4), 81–100. doi:10.1080/10641197709379771

Gross, D., and Seelig, T. (2017). *Fracture Mechanics: With an Introduction to Micromechanics*. 3rd ed. Berlin: Springer.

Haeckel, M., Suess, E., Wallmann, K., and Rickert, D. (2004). Rising Methane Gas Bubbles Form Massive Hydrate Layers at the Seafloor. *Geochimica et Cosmochimica Acta* 68, 4335–4345. doi:10.1016/j.gca.2004.01.018

Hofmann, H., Lorke, A., and Peeters, F. (2008). The Relative Importance of Wind and Ship Waves in the Littoral Zone of a Large lake. *Limnol. Oceanogr.* 53 (1), 368–380. doi:10.4319/lo.2008.53.1.0368

Hovland, M., Gardner, J. V., and Judd, A. G. (2002). The Significance of Pockmarks to Understanding Fluid Flow Processes and Geohazards. *Geofluids* 2 (2), 127–136. doi:10.1046/j.1468-8123.2002.00028.x

Jain, A. K., and Juanes, R. (2009). Preferential Mode of Gas Invasion in Sediments: Grain-Scale Mechanistic Model of Coupled Multiphase Fluid Flow and Sediment Mechanics. *J. Geophys. Res.* 114, B08101. doi:10.1029/2008JB006002

Johnson, B. D., Boudreau, B. P., Gardiner, B. S., and Maass, R. (2002). Mechanical Response of Sediments to Bubble Growth. *Mar. Geology.* 187 (3-4), 347–363. doi:10.1016/S0025-3227(02)00383-3

Katsman, R. (2015). Correlation of Shape and Size of Methane Bubbles in fine-grained Muddy Aquatic Sediments with Sediment Fracture Toughness. *J. Struct. Geology.* 70, 56–64. doi:10.1016/j.jsg.2014.11.002

Katsman, R. (2019). Methane Bubble Escape from Gas Horizon in Muddy Aquatic Sediment under Periodic Wave Loading. *Geophys. Res. Lett.* 46 (12), 6507–6515. doi:10.1029/2019GL083100

Katsman, R., Ostrovsky, I., and Makovsky, Y. (2013). Methane Bubble Growth in fine-grained Muddy Aquatic Sediment: Insight from Modeling. *Earth Planet. Sci. Lett.* 377-378, 336–346. doi:10.1016/j.epsl.2013.07.011

Keller, M., and Stallard, R. F. (1994). Methane Emission by Bubbling from Gatun Lake, Panama. *J. Geophys. Res.* 99 (D4), 8307–8319. doi:10.1029/92JD02170

Kirschke, S., Bousquet, P., Ciais, P., Saunois, M., Canadell, J. G., Dlugokencky, E. J., et al. (2013). Three Decades of Global Methane Sources and Sinks. *Nat. Geosci* 6, 813–823. doi:10.1038/ngeo1955

Lawn, B. R. (1993). *Fracture of Brittle Solids*. 2nd ed. New York: Cambridge University Press.

Liu, L., Sotiri, K., Dück, Y., Hilgert, S., Ostrovsky, I., Uzhansky, E., et al. (2020). The Control of Sediment Gas Accumulation on Spatial Distribution of Ebullition in Lake Kinneret. *Geo-mar Lett.* 40 (4), 453–466. doi:10.1007/s00367-019-00612-z

Martens, C. S., and Berner, R. A. (1977). Interstitial Water Chemistry of Anoxic Long Island Sound Sediments. 1. Dissolved Gases1. *Limnol. Oceanogr.* 22 (1), 10–25. doi:10.4319/lo.1977.22.1.0010

Martens, C. S. (1976). Control of Methane Sediment-Water Bubble Transport by Macroinfaunal Irrigation in Cape Lookout Bight, North Carolina. *Science* 192 (4243), 998–1000. doi:10.1126/science.192.4243.998

Martens, C. S., and Val Klump, J. (1980). Biogeochemical Cycling in an Organic-Rich Coastal marine basin-I. Methane Sediment-Water Exchange Processes. *Geochimica et Cosmochimica Acta* 44 (3), 471–490. doi:10.1016/0016-7037(80)90045-9

Mattson, M. D., and Likens, G. E. (1990). Air Pressure and Methane Fluxes. *Nature* 347 (6295), 718–719. doi:10.1038/347718b0

Miller, L. G., and Oremland, R. S. (1988). Methane Efflux from the Pelagic Regions of Four Lakes. *Glob. Biogeochem. Cycles* 2 (3), 269–277. doi:10.1029/GB002i003p00269

Mitchell, J. K., and Soga, K. (2005). *Fundamentals of Soil Behavior*. 3rd ed. Hoboken, New Jersey: John Wiley & Sons.

Nageswaran, S. (1983). *Effect of Gas Bubbles on the Seabed Behaviour*. Oxford, England: Oxford University. PhD thesis.

NEN (1989). *Geotechniek - Classificatie Van Onverharde Grondmonsters, NEN 5104*. Delft: Nederlands Normalisatie-instituut.

Ostrovsky, I., and Tęgowski, J. (2010). Hydroacoustic Analysis of Spatial and Temporal Variability of Bottom Sediment Characteristics in Lake Kinneret in Relation to Water Level Fluctuation. *Geo-mar Lett.* 30 (3), 261–269. doi:10.1007/s00367-009-0180-4

Reed, A. H., Boudreau, B. P., Algar, C., and Furukawa, Y. (2005). "Morphology of Gas Bubbles in Mud: A Microcomputed Tomographic Evaluation," in Proceedings of The International Conference "Underwater Acoustic Measurements: Technologies & Results", Heraklion, Crete, Greece, 28th June -1st July 2005. https://apps.dtic.mil/sti/citations/ADA454883.

Römer, M., Riedel, M., Scherwath, M., Heesemann, M., and Spence, G. D. (2016). Tidally Controlled Gas Bubble Emissions: A Comprehensive Study Using Long-Term Monitoring Data from the NEPTUNE Cabled Observatory Offshore Vancouver Island. *Geochem. Geophys. Geosyst.* 17 (9), 3797–3814. doi:10.1002/2016GC006528

Saunois, M., Bousquet, P., Poulter, B., Peregon, A., Ciais, P., Canadell, J. G., et al. (2016). The Global Methane Budget 2000–2012. *Earth Syst. Sci. Data* 8 (2), 697–751. doi:10.5194/essd-8-697-2016

Scandella, B. P., Delwiche, K., Hemond, H. F., and Juanes, R. (2017). Persistence of Bubble Outlets in Soft, Methane-generating Sediments. *J. Geophys. Res. Biogeosci.* 122 (6), 1298–1320. doi:10.1002/2016JG003717

Scandella, B. P., Pillsbury, L., Weber, T., Ruppel, C., Hemond, H. F., and Juanes, R. (2016). Ephemerality of Discrete Methane Vents in lake Sediments. *Geophys. Res. Lett.* 43 (9), 4374–4381. doi:10.1002/2016GL068668

Scandella, B. P., Varadharajan, C., Hemond, H. F., Ruppel, C., and Juanes, R. (2011). A Conduit Dilation Model of Methane Venting from lake Sediments. *Geophys. Res. Lett.* 38 (6), L06408. doi:10.1029/2011GL046768

Serruya, S. (1975). Wind, Water Temperature and Motions in Lake Kinneret: General Pattern. *SIL Proc* 19 (1), 73–87. doi:10.1080/03680770.1974.11896041

Sevee, J. E. (2010). Effective Porosity Measurement of a marine clay. *J. Environ. Eng.* 136 (7), 674–681. doi:10.1061/(ASCE)EE.1943-7870.0000205

Shin, H., and Santamarina, J. C. (2010). Fluid-driven Fractures in Uncemented Sediments: Underlying Particle-Level Processes. *Earth Planet. Sci. Lett.* 299 (1-2), 180–189. doi:10.1016/j.epsl.2010.08.033

Sills, G. C., and Wheeler, S. J. (1992). The Significance of Gas for Offshore Operations. *Continental Shelf Res.* 12 (10), 1239–1250. doi:10.1016/0278-4343(92)90083-V

Sills, G. C., Wheeler, S. J., Thomas, S. D., and Gardner, T. N. (1991). Behaviour of Offshore Soils Containing Gas Bubbles. *Géotechnique* 41 (2), 227–241. doi:10.1680/geot.1991.41.2.227

Sirhan, S. T., Katsman, R., and Lazar, M. (2019). Methane Bubble Ascent within fine-grained Cohesive Aquatic Sediments: Dynamics and Controlling Factors. *Environ. Sci. Technol.* 53 (11), 6320–6329. doi:10.1021/acs.est.8b06848

T. Zohary, A. Sukenik, T. Berman, and A. Nishri (Editors) (2014). *Lake Kinneret: Ecology and Management* (New York, Heidelberg, Dordrecht and London: Springer), 6.

USEPA (2010). *Methane and Nitrous Oxide Emissions from Natural Sources*. Washington DC: US Environmental Protection Agency. EPA 430-R-10–001.

Uzhansky, E., Katsnelson, B., Lunkov, A., and Ostrovsky, I. (2020). Spatial and Temporal Variability of Free Gas Content in Shallow Sediments: Lake Kinneret as a Case Study. *Geo-mar Lett.* 40 (4), 491–505. doi:10.1007/s00367-019-00629-4

Van Kessel, T., and Van Kesteren, W. G. M. (2002). Gas Production and Transport in Artificial Sludge Depots. *Waste Manag.* 22 (1), 19–28. doi:10.1016/S0956-053X(01)00021-6

Van Kesteren, W., and van Kessel, T. (2002). "Gas Bubble Nucleation and Growth in Cohesive Sediments," in *Finite Sediment Dynamics in the marine Environment*. Proceedings in Marine Science. Editors J. C. Winterwerp and C. Kranenburg (Amsterdam: Elsevier), 5 329–341. doi:10.1016/s1568-2692(02)80025-0

Wheeler, S. J. (1988). A Conceptual Model for Soils Containing Large Gas Bubbles. *Géotechnique* 38 (3), 389–397. doi:10.1680/geot.1988.38.3.389

Wheeler, S. J. (1990). Movement of Large Gas Bubbles in Unsaturated fine-grained Sediments. *Mar. Geotechnology* 9 (2), 113–129. doi:10.1080/10641199009388234

Winterwerp, J. C., and van Kesteren, W. G. M. (2004). *Introduction to the Physics of Cohesive Sediment Dynamics in the marine Environment*, 6. Amsterdam, Netherlands: Elsevier.

Zamanpour, M. K., Kaliappan, R. S., and Rockne, K. J. (2020). Gas Ebullition from Petroleum Hydrocarbons in Aquatic Sediments: A Review. *J. Environ. Manage.* 271, 110997. doi:10.1016/j.jenvman.2020.110997

Conflict of Interest: The authors declare that the research was conducted in the absence of any commercial or financial relationships that could be construed as a potential conflict of interest.

Publisher's Note: All claims expressed in this article are solely those of the authors and do not necessarily represent those of their affiliated organizations, or those of the publisher, the editors, and the reviewers. Any product that may be evaluated in this article, or claim that may be made by its manufacturer, is not guaranteed nor endorsed by the publisher.